Quantized Born Effective charges as probes for the topological phase transition in the Haldane and Kane-Mele models

Paolo Fachin,[1] Francesco Macheda,[1] Paolo Barone,[2,1] and Francesco Mauri[1]

[1] *Dipartimento di Fisica, Università di Roma La Sapienza, Roma, Italy*
[2] *CNR-SPIN, Area della Ricerca di Tor Vergata, Via del Fosso del Cavaliere 100, I-00133 Rome, Italy*

We propose a new approach to study the transition between different topological states, based on the assessment of the vibrational resonances in infrared spectra. We consider the Haldane and Kane-Mele models finding that Born effective charges are nearly quantized, with a discontinuous jump concomitant with the topological phase transition. In particular, Born effective charges display a finite value in the trivial phase and a null one in the nontrivial one. This is rooted in the connection between Born effective charges and electronic Berry curvature at the band edges. Finally, at the topological phase transition of the Haldane model, we also observe a nearly quantized jump of the chiral splitting of the zone-center phonon frequencies, induced by time-reversal symmetry breaking.

Introduction— Chiral phonons have recently been observed in non-equilibrium phases of topologically trivial states by using circularly polarized light carrying angular momentum [1–3]. An equilibrium, intrinsic, chiral nature of phonons originates by the breaking of time-reversal symmetry [4]. Here, the molecular Berry curvature induces an anomalous contribution to the phonon eigenvalue equation acting as an effective classical Lorentz force, that breaks the energetic equivalence between differently polarized phonons at zone center [5–8]. Intrinsic chiral phonons have been related to the nontrivial topology of the Haldane model [5], a prototype for the Quantum Anomalous Hall (QAH) insulating state [9]. Indeed, chiral phonon splittings have been proposed as experimental markers for transitions to topological phases not protected by time-reversal symmetry [10]. On the other hand, the detection of topological nontrivial states in systems displaying time-reversal, such as the Quantum Spin Hall (QSH) states [11, 12], has been based so far on either charge transport measurements probing the longitudinal resistance in Hall bar geometry [13–15] or discriminating conductive edge states from insulating bulk by directly imaging the local conductivity [16–22]. Only recently discontinuous changes of piezoelectric response have been theoretically suggested as direct probes of topological transitions in 2D time-reversal invariant systems [23, 24].

In this work, we propose a different measurable quantity to detect the transition between trivial and nontrivial topological phases of matter, namely the Born effective charges. Quantifying the polarization change due to atomic displacements, Born effective charges can be experimentally accessed, e.g., from the mode oscillator strengths of vibrational resonances in infrared spectra [25]. We first investigate their properties for the Haldane model where time-reversal is broken by complex next-nearest-neighbor hoppings [26]. We find that Born effective charges display nearly quantized values in the trivial phase, while they almost vanish in the nontrivial one, at odds with chiral phonon splitting displaying an opposite dependence on topology [5]. This behaviour is well understood via a low-energy expansion of the Haldane model, where the Born effective charge is determined by the difference of Chern numbers evaluated at non-equivalent **K** and **K'** points, while the chiral phonon splitting depends on their sum. Superimposing two Haldane models with opposite next-nearest-neighbor hopping restores time-reversal symmetry, thus preventing the occurrence of chiral phonon splitting in the whole phase diagram; still, Born effective charges display quantized jump between different phases. A realistic realization of a topological system retaining time-reversal symmetry is the Kane-Mele model [11] that includes a Rashba coupling term induced either by a perpendicular electric field or by the interaction with a substrate, for which we numerically confirm that the Born effective charge can be used as a marker to individuate the onset of the $\mathcal{Z}_2$ topological order, corresponding to the QSH insulator [27]. Among the recently proposed materials realizing the Kane-Mele model, germanene has been shown to host a QSH state at experimentally accessible temperatures, with a topological transition to a trivial state induced by a critical perpendicular electric field $E_{z,c} \sim 1.95$ V/nm [22]. Jacutingaite, a natural occurring layered and exfoliable mineral, has also been predicted to host a large-gap QSH state when in monolayer form, also tunable by an applied perpendicular field [28]. Our proposal could as well be relevant for the experimental investigation of 3D weak topological insulators comprising weakly coupled QSH monolayers, whose topological surfaces are usually not cleavable and hard to access using standard surface-sensitive techniques [29, 30].

Berry curvatures— The relationship between topological properties, Born effective charges and chiral phonons can be rationalized in terms of Berry curvatures, encoding the geometric properties of electronic wavefunctions in a crystal. In a periodic crystal the electronic and nuclear degrees of freedom can be decoupled following the Born-Oppenheimer approximation. The nuclei are located at

their positions $\boldsymbol{u}_s(\boldsymbol{R}) = \boldsymbol{R} + \boldsymbol{\tau}_s$, where $\boldsymbol{R}$ is a Bravais lattice vector and $\boldsymbol{\tau}_s$ indicates the position of the atom s within the cell. The electrons are then described in a mean field framework by a single-particle Hamiltonian $H_{\boldsymbol{k}}$, $\boldsymbol{k}$ being the quasi-momentum, which parametrically depends on the atomic positions. For a generic couple of parameters (ζ, λ), we define the Berry curvature of the occupied manifold as [31–34]

$$\begin{aligned}\Omega_{\zeta\lambda}(\boldsymbol{k}) &= -2\mathrm{Im}\sum_{n}^{\mathrm{occ}} \langle \partial_\zeta \upsilon_{n\boldsymbol{k}} | \partial_\lambda \upsilon_{n\boldsymbol{k}} \rangle \\ &= -2\mathrm{Im}\sum_{n}^{\mathrm{occ}}\sum_{m}^{\mathrm{empty}} \frac{\langle \upsilon_{n\boldsymbol{k}} | \partial_\zeta H_{\boldsymbol{k}} | \upsilon_{m\boldsymbol{k}} \rangle \langle \upsilon_{m\boldsymbol{k}} | \partial_\lambda H_{\boldsymbol{k}} | \upsilon_{n\boldsymbol{k}} \rangle}{(\varepsilon_{n\boldsymbol{k}} - \varepsilon_{m\boldsymbol{k}})^2},\end{aligned} \tag{1}$$

where $\varepsilon_{n\boldsymbol{k}}$ and $|\upsilon_{n\boldsymbol{k}}\rangle$ are the eigenvalues and eigenfunctions of $H_{\boldsymbol{k}}$, and the sum over n and m run on the manifold of occupied and empty bands, respectively. If ζ and λ are atomic positions, then Eq. 1 determines the molecular Berry curvature of the system. As shown in Ref. [5] for the Haldane model, the molecular Berry manifests as a non-local effective magnetic field in the equations of motion of the ion [35], inducing a chiral splitting of the zone-center phonon frequencies. The anomalous contribution to the phonon eigenvalue equation at zone center is, in the limit where the phonon frequency is much smaller than the band gap [7], proportional to

$$F_{s\alpha,r\beta} = \frac{\hbar^2}{\sqrt{M_s M_r}} \frac{A}{(2\pi)^2} \int_{\mathrm{BZ}} d^2\boldsymbol{k}\, \Omega_{u_{s\alpha}u_{r\beta}}(\boldsymbol{k}), \tag{2}$$

where r, s are atomic indexes and $\alpha, \beta = x, y$ are Cartesian coordinates, $M_{s/r}$ the ion masses and A is the unit cell area. $u_{s\alpha}$ is an atomic displacement equal in each cell of the crystal, so that the $\boldsymbol{R}$ dependence is dropped.

Beside the atomic positions, $H_{\boldsymbol{k}}$ is also parametrically dependent on the quasi-momentum. If we identify ζ and λ with the quasi-momentum, Eq. 1 then describes the electronic Berry curvature. This is related to nontrivial topological properties, such as the QAH Conductivity, via the total Chern number [31, 36]

$$C = \frac{1}{2\pi} \int_{\mathrm{BZ}} d^2\boldsymbol{k}\, \Omega_{k_x k_y}(\boldsymbol{k}). \tag{3}$$

The mixed derivative where ζ is the quasi-momentum and λ is the atomic position is instead related to the static Born effective charge tensor, that can be expressed in the same limit where the phonon frequency is much smaller than the band gap, as [37]

$$Z^*_{s,\beta\alpha} = \frac{A}{(2\pi)^2} \int_{\mathrm{BZ}} d^2\boldsymbol{k}\, \Omega_{k_\alpha u_{s\beta}}(\boldsymbol{k}). \tag{4}$$

While great attention has been devoted to the study of the molecular and electronic Berry curvatures for materials displaying topological properties, little attention has been given in this context to the mixed derivative of Eq. 4, that will be the focus of this work.

Haldane Model— We consider the Haldane model, described by a tight-binding spinless Hamiltonian on a 2D honeycomb lattice with two atoms per unit cell [38], one atomic orbital per atom and one electron in each orbital

$$H = \frac{\Delta}{2}\sum_i l_i c_i^\dagger c_i + t_1 \sum_{\langle ij \rangle} c_i^\dagger c_j + i t_2 \sum_{\langle\langle ij \rangle\rangle} l_{ij} c_i^\dagger c_j. \tag{5}$$

$c_i, c_i^\dagger$ are the electronic creation and annihilation operators, where i is a short-hand notation indicating both the cell and the sublattice index. $\Delta/2$ is the on-site energy, t_1 and t_2 are real quantities and $l_i = 1, -1$ is the sublattice index of the site i. $\langle\rangle$ means sum on first nearest neighbours and $\langle\langle\rangle\rangle$ on the second ones. Each term in the sum over $\langle\langle\rangle\rangle$ enters with a sign $l_{ij} = 1, -1$, determined accordingly to the direction of the vector connecting the sites [26, 31]. We adopt the lattice parameter and t_1 hopping parameters of graphene, i.e. $a = 2.46$ Å and $t_1 = 3.4$eV [39], and the atomic masses are the ones of carbon, for which we set $M_s = M$.

The model describes a two-band system with broken time-reversal symmetry due to the imaginary next-nearest-neighbors hopping term it_2. One band is occupied and one is empty, so that we can easily drop the summation over electronic states. The topological phase diagram of the Haldane model in the parameter space $(\Delta/t_1, t_2/t_1)$ is represented in the bottom panel of Figure 1, where the trivial and nontrivial phases are identified by the total Chern number being $C = 0$ and $C = \pm 1$, respectively, as computed via Eq. 3. The phases are separated by a metallic state, where the gap closes. The coupling between electrons and lattice vibrations is obtained considering the variation of the hopping constants following an atomic displacement. We assume that only the t_1 term contributes to the electron-phonon coupling, and that the variation of t_1 depends only on longitudinal bond stretchings. The electron-phonon interaction for zone-center lattice vibrations can then be quantified by the coupling parameter ξ [40] as [39, 41–43]

$$\delta H_{\text{e-ph}} = -t_1 \xi \sum_{\langle ij \rangle} \boldsymbol{b}_{ij} \cdot (\delta \boldsymbol{u}_j - \delta \boldsymbol{u}_i)\, c_i^\dagger c_j. \tag{6}$$

Here $\boldsymbol{b}_{ij} = \boldsymbol{u}_j - \boldsymbol{u}_i$ is the vector connecting the sites i and j, while the coupling constant is set to the value obtained for graphene, $\xi = 1.2$ Å^{-2}.

Beside the electronic properties, the nontrivial topology also affects the ion dynamics. In particular, in the nontrivial phases the double degenerate optical phonon modes at the $\boldsymbol{\Gamma}$ point split into two circularly polarized modes with opposite chirality and different energies [5]. For anomalous contributions that are small with respect to the dynamical matrix, the phonon splitting is given by $\Delta\omega = 2|F_{sx,sy}|$ ([5]). The full $F_{s\alpha,r\beta}$ matrix further contains the information of which chiral phonon is highest in

energy. For this reason, we consider for each atom s the quantity $F_{sx,sy} = l_s \mathcal{F}$. As shown in the upper panel of Fig. 1, $\mathcal{F}$ is almost null in the trivial topological phase, while it displays a finite and fairly constant value in different nontrivial ones, with an almost quantized jump in correspondence with the metallic phase. The sign of $\mathcal{F}$ changes when passing from the $C = 1$ to the $C = -1$ phases, i.e., when changing the t_2 sign. Finally, we study Eq. 4 for the Haldane model. Due to symmetry and charge neutrality, the Born effective charge tensor can be written as $Z^*_{s,\alpha\beta} = Z^* l_s \delta_{\alpha\beta}$. As shown in the central panel of Fig. 1, Z^* appears as almost quantized, with a nearly vanishing values in the nontrivial phase and a finite value in the trivial one. The value of Z^* changes when reversing the Δ sign. Interestingly, the nearly quantization of Z^* extends to larger portions of the topological space as compared to $\mathcal{F}$.

The above results are rationalized thanks to a low-energy expansion of the tight-binding model. This approximation holds well for small gap values such that the Berry curvatures are mostly localized around **K** and **K'** points in reciprocal space [38, 44]. Therefore, the observables are expected to closely follow the predictions of the low-energy model, which we obtain by expanding the Hamiltonian for small quasi-momenta $\boldsymbol{p}$ around the non-equivalent **K** and **K'**. We refer to the sets of points near **K** and **K'** as belonging to different 'valleys', labeling them as D_η with $\eta = \pm 1$. In this description, the coupling between electrons and phonons can be expressed as a 'gauge' field

$$\boldsymbol{\mathcal{A}} = \sum_s \boldsymbol{\mathcal{A}}_s, \quad \boldsymbol{\mathcal{A}}_s = l_s \hat{\boldsymbol{z}} \times \delta \boldsymbol{u}_s. \tag{7}$$

$\boldsymbol{\mathcal{A}}$ enters the low-energy Hamiltonian of each valley η mimicking a minimal coupling [44, 45], as

$$H_\eta = \hbar v_{\mathrm{F}} \left(\eta p_x + \xi \mathcal{A}_x, p_y + \eta \xi \mathcal{A}_y, \frac{\Delta/2 - \eta 3\sqrt{3} t_2}{\hbar v_{\mathrm{F}}} \right) \cdot \boldsymbol{\sigma}^{\mathrm{P}}, \tag{8}$$

where $\hbar v_{\mathrm{F}} = \frac{\sqrt{3} t_1 a}{2}$ and $\boldsymbol{\sigma}^{\mathrm{P}} = (\sigma^{\mathrm{P}}_x, \sigma^{\mathrm{P}}_y, \sigma^{\mathrm{P}}_z)$ is the vector of Pauli matrices in the pseudospin space, the two pseudo-spinor components corresponding to the amplitude of the periodic part of the Bloch state $|v_{n\boldsymbol{k}}\rangle$ on the two atom sites in the unit cell [32].

For the low-energy model, the integration over all the Brillouin zone is replaced by the sum of the two valleys integrals as $\int_{\mathrm{BZ}} d^2\boldsymbol{k} \to \sum_{\eta=\pm1} \int_{D_\eta} d^2\boldsymbol{p}$. Then, the Chern number of Eq. 3 is expressed as the sum of two valley Chern numbers $C_\eta = \frac{1}{2\pi} \int_{D_\eta} d^2\boldsymbol{p}\, \Omega_{p_x p_y}(\boldsymbol{p})$ as

$$C = \sum_{\eta=\pm1} (\eta)^0 C_\eta. \tag{9}$$

In the trivial phase the valley fraction Chern numbers are $C_\eta = \mathrm{sign}(\Delta)\frac{\eta}{2}$ and cancel out in the sum, while in the topological phase they are both equal to $C_\eta = \mathrm{sign}(t_2)\frac{1}{2}$. To evaluate also Z^* and $\mathcal{F}$, we notice that in the low-energy model of Eq. 8 the derivative with respect to the phonon perturbation transforms in the derivative with

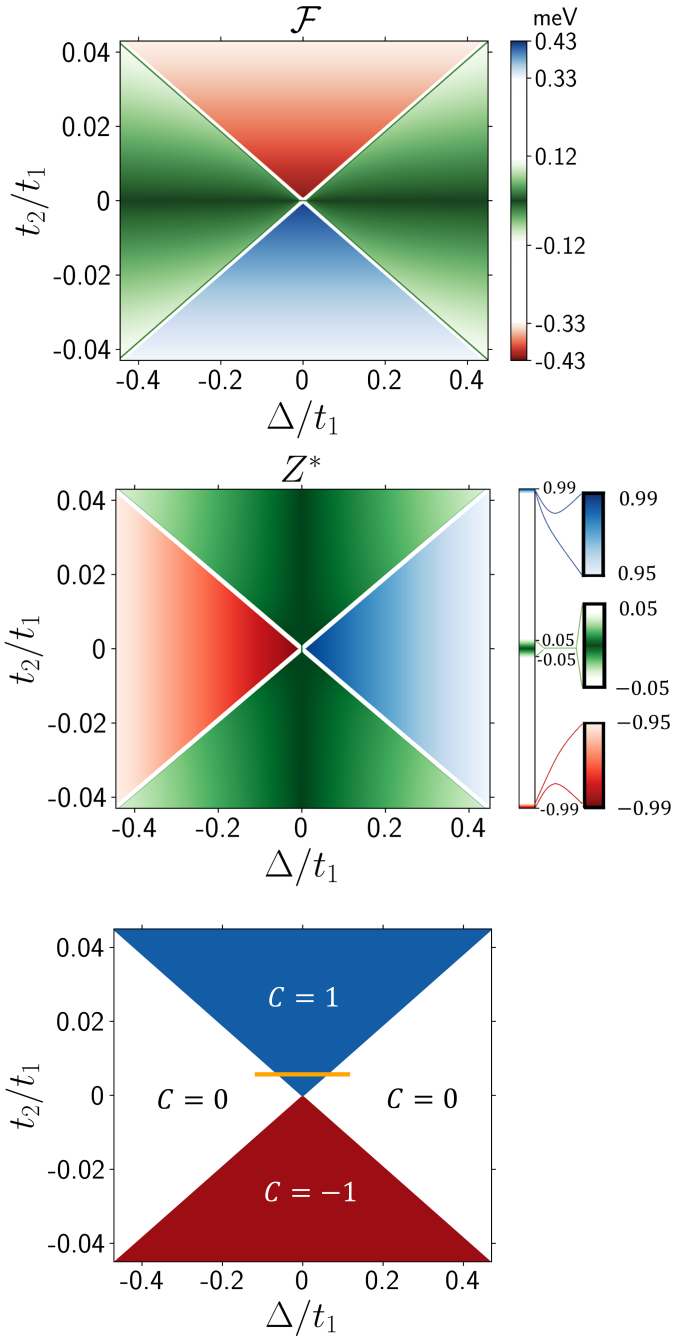

FIG. 1. (Upper) $\mathcal{F}$ and (middle) Z^* display nearly quantized values in topologically different zones of the phase diagram of the Haldane model in the plane $(\Delta/t_1, t_2/t_1)$ for $t_1 = 3.4$ eV. (Lower) Analytical topological phase diagram of the Haldane model. The horizontal orange line corresponds to the region of parameter space further expanded in Fig. 2.

respect to the crystalline quasi-momentum as

$$\frac{\partial H_{\boldsymbol{p}}}{\partial u_{sx}} = l_s \frac{\partial H_{\boldsymbol{p}}}{\partial A_{sy}} = l_s \eta \xi \frac{\partial H_{\boldsymbol{p}}}{\partial p_y}, \tag{10}$$

$$\frac{\partial H_{\boldsymbol{p}}}{\partial u_{sy}} = -l_s \frac{\partial H_{\boldsymbol{p}}}{\partial A_{sx}} = -l_s \eta \xi \frac{\partial H_{\boldsymbol{p}}}{\partial p_x}. \tag{11}$$

As a consequence, Z^* and $\mathcal{F}$ are directly related to the electronic Berry curvatures, and thus to the Chern number, as

$$Z^* = \frac{A}{2\pi} \xi \sum_{\eta=\pm 1} (\eta)^1 C_\eta = \mathrm{sign}(\Delta) \frac{A}{2\pi} \xi (1 - |C|), \tag{12}$$

$$\mathcal{F} = -\frac{\hbar^2}{M} \frac{A}{2\pi} (\xi)^2 \sum_{\eta=\pm 1} (\eta)^2 C_\eta = -\frac{\hbar^2}{M} \frac{A}{2\pi} (\xi)^2 C. \tag{13}$$

Moreover, the Born Effective charges provide a direct measure of the valley Chern number $C_V = \sum_\eta \eta C_\eta$ [44]. Hence, the nearly quantized properties for the Haldane model are almost all due to the topological properties of its low-energy model, and as such they are quite robust to modification of the electronic band structure, as shown also in the SI [38]. Notice that C, Z^* and $\mathcal{F}$ are written in the low-energy model as sums over growing powers of η. Substituting both phonon derivatives with electronic ones for $\mathcal{F}$ results in an higher degree of approximation in the description of the tight-binding model and, thus, in a less pronounced quasi quantization with respect to the Z^*. The result for $\mathcal{F}$ is in agreement with Ref. [5].

Kane-Mele model— In the Haldane model describing spinless electrons the time-reversal symmetry operation on the Hamiltonian corresponds to the change of the sign of t_2. The inversion symmetry, on the other hand, is equivalent to a sign change of the onsite energy Δ. As plotted in Figure 1, both C and $\mathcal{F}$ change sign under the time-reversal symmetry operation, while Z^* is invariant. The behaviour with respect to the inversion symmetry is opposite, since C and $\mathcal{F}$ are invariant while Z^* changes sign. By combining two Haldane models with opposite sign of t_2, i.e., two time-reversed copies of the system, we expect Z^* to sum up and C and $\mathcal{F}$ to vanish. This system actually coincide with the Kane-Mele model without Rashba coupling [11, 46], with a proper identification of the spin-orbit coupling term with t_2. Here, the two time-reversed copies of the Haldane model correspond to the two different $\uparrow$ and $\downarrow$ spin components of the system, each copy displaying a Chern number such that $C_\uparrow = -C_\downarrow$ as a consequence of time-reversal symmetry. In spite of displaying a null total Chern number, the Kane-Mele model still presents a topologically nontrivial phase according to the $\mathcal{Z}_2$ classification [27]. It follows that the low-energy expression of the Born effective charge in the Kane-Mele model without Rashba coupling reads:

$$Z^* = \mathrm{sign}(\Delta) \frac{A}{2\pi} \xi (2 - |C_\uparrow| - |C_\downarrow|). \tag{14}$$

We then expect Z^* to retain its nearly quantized value discerning between the trivial and the nontrivial $\mathcal{Z}_2$ topological phases, in analogy of what happens for the $\mathcal{Z}$ topological Haldane model.

A full description of the Kane-Mele model requires the inclusion of the Rashba term, mixing spin components. Introducing the coupling constant λ_{R}, the Rashba coupling reads:

$$H_{\mathrm{R}} = i\lambda_{\mathrm{R}} \sum_{\langle ij \rangle, \rho\rho'} l_i \, c^\dagger_{i\rho} \left[\left(\hat{\boldsymbol{b}}_{ij} \times \hat{\boldsymbol{z}} \right) \cdot \boldsymbol{\sigma}^{\mathrm{S}} \right]_{\rho\rho'} c_{j\rho'}, \tag{15}$$

where ρ, ρ' are spin indexes, $\hat{\boldsymbol{b}}_{ij}$ is the nearest neighbour distance normalized to the unity, $\boldsymbol{\sigma}^{\mathrm{S}} = (\sigma^{\mathrm{S}}_x, \sigma^{\mathrm{S}}_y, \sigma^{\mathrm{S}}_z)$ is the vector containing Pauli matrices in spin space. Being time-reversal symmetric, the Rashba term preserves the topological properties as long as the system is adiabatically connected to the QSH phase at $\lambda_R = 0$, i.e., until the band-gap closes [27]. Acting on λ_{R}, e.g. by applying a perpendicular electric field, the system can be driven from the topological to the trivial phase and viceversa by crossing the metallic line, as shown in the lower panel of Fig. 2 for $t_2 = 0.02$ eV. The corresponding evolution of Z^* is displayed in the upper panel, confirming the expected nearly quantized behavior of the effective charge. We numerically checked the relationship between Born effective charge, valley Chern number and the topological index $\mathcal{Z}_2$, as shown in SI [38].

Discussion and conclusions— We showed that the Born effective charges display an almost quantized jump between different topological phases in the Haldane and Kane-Mele models by virtue of their direct relation with the valley Chern number. We infer that two conditions need to be met for such relation to hold: i) the electronic Berry curvature being mostly localized around valley points, such that valley Chern numbers are well defined and meaningful quantities; and ii) the electron-phonon coupling being effectively described by a gauge field, such that both molecular and mixed Berry curvatures, accounting for chiral phonon splitting and Born effective charges respectively, can be expressed in terms of electronic Berry curvature. We remark that, at odds with "deformation potential" contributions to electron-phonon interaction, gauge-field terms are unaffected by electronic screening [43], hinting to further robustness of the proposed effect. Finally, we emphasize the analogy with the predicted discontinuous changes of piezoelectric response in 2D time-reversal invariant systems, recently proposed as experimental markers of topological transitions [23, 24], also relying on well-defined valley Chern numbers and on the electron-strain coupling acting as a gauge field [44, 47, 48].

Acknowledgments— We acknowledge the MORE-TEM ERC-SYN project, grant agreement no. 95121. We acknowledge the EuroHPC Joint Undertaking for awarding this project access to the EuroHPC supercomputer

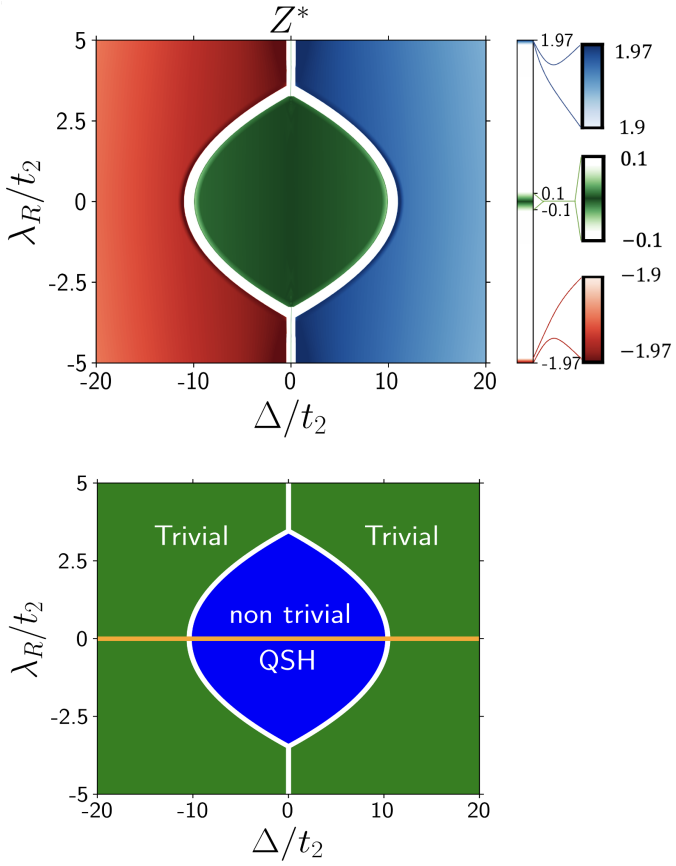

FIG. 2. (Upper) Z^* with nearly quantized values in the topologically different regions of the phase diagram of the Kane-Mele model in the $(\Delta/t_2, \lambda_R/t_2)$ plane for $t_2 = 0.02$ eV. We set t_2 as the energy unit to ease the comparison with Ref. [27]. (Lower) Numerical topological phase diagram of the Kane-Mele model. The blue region indicates where QSH is realized. The white region numerically identifies band gaps close to metallization. The parameters indicated by the horizontal orange line are the same of the orange line of Fig. 1, where we adopted t_1 as the energy unit; the Rashba coupling is zero along this line, and the Kane-Mele model reduces to two time-reversal related copies of the Haldane model.

LUMI, hosted by CSC (Finland) and the LUMI consortium through a EuroHPC Regular Access call.

[1] J. Luo, T. Lin, J. Zhang, X. Chen, E. R. Blackert, R. Xu, B. I. Yakobson, and H. Zhu, Large effective magnetic fields from chiral phonons in rare-earth halides, Science **382**, 698 (2023), https://www.science.org/doi/pdf/10.1126/science.adi9601.

[2] H. Ueda, M. García-Fernández, S. Agrestini, C. P. Romao, J. van den Brink, N. A. Spaldin, K.-J. Zhou, and U. Staub, Chiral phonons in quartz probed by x-rays, Nature **618**, 946 (2023).

[3] H. Zhu, J. Yi, M.-Y. Li, J. Xiao, L. Zhang, C.-W. Yang, R. A. Kaindl, L.-J. Li, Y. Wang, and X. Zhang, Observation of chiral phonons, Science **359**, 579 (2018), https://www.science.org/doi/pdf/10.1126/science.aar2711.

[4] S. Coh, Classification of materials with phonon angular momentum and microscopic origin of angular momentum, Phys. Rev. B **108**, 134307 (2023).

[5] D. Saparov, B. Xiong, Y. Ren, and Q. Niu, Lattice dynamics with molecular berry curvature: Chiral optical phonons, Phys. Rev. B **105**, 064303 (2022).

[6] J. Bonini, S. Ren, D. Vanderbilt, M. Stengel, C. E. Dreyer, and S. Coh, Frequency splitting of chiral phonons from broken time-reversal symmetry in cri_3, Phys. Rev. Lett. **130**, 086701 (2023).

[7] O. Bistoni, F. Mauri, and M. Calandra, Intrinsic vibrational angular momentum from nonadiabatic effects in noncollinear magnetic molecules, Phys. Rev. Lett. **126**, 225703 (2021).

[8] S. Ren, J. Bonini, M. Stengel, C. E. Dreyer, and D. Vanderbilt, Adiabatic dynamics of coupled spins and phonons in magnetic insulators, Phys. Rev. X **14**, 011041 (2024).

[9] C.-X. Liu, S.-C. Zhang, and X.-L. Qi, The Quantum Anomalous Hall Effect: Theory and Experiment, Annual Review of Condensed Matter Physics **7**, 301 (2016).

[10] F. G. Hernandez, A. Baydin, S. Chaudhary, F. Tay, I. Katayama, J. Takeda, H. Nojiri, A. K. Okazaki, P. H. Rappl, E. Abramof, M. Rodriguez-Vega, G. A. Fiete, and J. Kono, Observation of interplay between phonon chirality and electronic band topology, Science Advances **9**, eadj4074 (2023), https://www.science.org/doi/pdf/10.1126/sciadv.adj4074.

[11] C. L. Kane and E. J. Mele, Quantum spin hall effect in graphene, Phys. Rev. Lett. **95**, 226801 (2005).

[12] B. A. Bernevig and S.-C. Zhang, Quantum spin hall effect, Phys. Rev. Lett. **96**, 106802 (2006).

[13] B. A. Bernevig, T. L. Hughes, and S.-C. Zhang, Quantum Spin Hall Effect and Topological Phase Transition in HgTe Quantum Wells, Science **314**, 1757 (2006), https://www.science.org/doi/pdf/10.1126/science.1133734.

[14] M. König, S. Wiedmann, C. Brüne, A. Roth, H. Buhmann, L. W. Molenkamp, X.-L. Qi, and S.-C. Zhang, Quantum spin hall insulator state in hgte quantum wells, Science **318**, 766 (2007), https://www.science.org/doi/pdf/10.1126/science.1148047.

[15] S. Wu, V. Fatemi, Q. D. Gibson, K. Watanabe, T. Taniguchi, R. J. Cava, and P. Jarillo-Herrero, Observation of the quantum spin hall effect up to 100 kelvin in a monolayer crystal, Science **359**, 76 (2018), https://www.science.org/doi/pdf/10.1126/science.aan6003.

[16] S. Tang, C. Zhang, D. Wong, Z. Pedramrazi, H.-Z. Tsai, *et al.*, Quantum spin hall state in monolayer $1T^{'} - WTe_2$, Nature Phys **13**, 683 (2017).

[17] Z.-Y. Jia, Y.-H. Song, X.-B. Li, K. Ran, P. Lu, H.-J. Zheng, X.-Y. Zhu, Z.-Q. Shi, J. Sun, J. Wen, D. Xing, and S.-C. Li, Direct visualization of a two-dimensional topological insulator in the single-layer $1T^{'} - WTe_2$, Phys. Rev. B **96**, 041108 (2017).

[18] F. Reis, G. Li, L. Dudy, M. Bauernfeind, S. Glass, W. Hanke, R. Thomale, J. Schäfer, and R. Claessen, Bismuthene on a SiC substrate: A candidate for a high-temperature quantum spin Hall material, Science **357**, 287 (2017).

[19] Y. Shi, J. Kahn, B. Niu, Z. Fei, B. Sun, X. Cai, B. A. Francisco, D. Wu, Z.-X. Shen, X. Xu, D. H. Cobden, and

Y.-T. Cui, Imaging quantum spin hall edges in monolayer WTe_2, Science Advances **5**, eaat8799 (2019).

[20] K. Kandrai, P. Vancsó, G. Kukucska, J. Koltai, G. Baranka, Á. Hoffmann, Á. Pekker, K. Kamarás, Z. E. Horváth, A. Vymazalová, L. Tapasztó, and P. Nemes-Incze, Signature of large-gap quantum spin hall state in the layered mineral jacutingaite, Nano Letters **20**, 5207 (2020).

[21] N. Shumiya, M. Hossain, J. Yin, W. Z., M. Litskevich, *et al.*, Evidence of a room-temperature quantum spin hall edge state in a higher-order topological insulator, Nature Mater **21**, 1111 (2022).

[22] P. Bampoulis, C. Castenmiller, D. J. Klaassen, J. van Mil, Y. Liu, C.-C. Liu, Y. Yao, M. Ezawa, A. N. Rudenko, and H. J. W. Zandvliet, Quantum spin hall states and topological phase transition in germanene, Phys. Rev. Lett. **130**, 196401 (2023).

[23] J. Yu and C.-X. Liu, Piezoelectricity and topological quantum phase transitions in two-dimensional spin-orbit coupled crystals with time-reversal symmetry, Nature Communications **11**, 2290 (2020).

[24] R. Peng and J. Liu, Topological piezoelectric response in moiré graphene systems, Phys. Rev. Res. **4**, L032006 (2022).

[25] M. Born and K. Huang, *Dynamical Theory of Crystal Lattices*, International series of monographs on physics (Clarendon Press, 1988).

[26] F. D. M. Haldane, Model for a quantum hall effect without landau levels: Condensed-matter realization of the "parity anomaly", Phys. Rev. Lett. **61**, 2015 (1988).

[27] C. L. Kane and E. J. Mele, Z_2 topological order and the quantum spin hall effect, Phys. Rev. Lett. **95**, 146802 (2005).

[28] A. Marrazzo, M. Gibertini, D. Campi, N. Mounet, and N. Marzari, Prediction of a large-gap and switchable kane-mele quantum spin hall insulator, Phys. Rev. Lett. **120**, 117701 (2018).

[29] M. Z. Hasan and C. L. Kane, Colloquium: Topological insulators, Rev. Mod. Phys. **82**, 3045 (2010).

[30] C. Pauly, B. Rasche, K. Koepernik, M. Liebmann, M. Pratzer, *et al.*, Subnanometre-wide electron channels protected by topology, Nature Phys **11**, 338 (2015).

[31] D. Vanderbilt, *Berry Phases in Electronic Structure Theory: Electric Polarization, Orbital Magnetization and Topological Insulators* (Cambridge University Press, 2018).

[32] G. Grosso and G. Pastori Parravicini, *Solid State Physics*, 2nd ed. (Academic Press, New York, USA, 2013).

[33] D. Xiao, M.-C. Chang, and Q. Niu, Berry phase effects on electronic properties, Rev. Mod. Phys. **82**, 1959 (2010).

[34] R. Resta, Macroscopic polarization in crystalline dielectrics: the geometric phase approach, Rev. Mod. Phys. **66**, 899 (1994).

[35] C. Mead and D. Truhlar, On the determination of born-oppenheimer nuclear motion wave functions including complications due to conical intersections and identical nuclei, The Journal of chemical physics **70**, 2284 (1979).

[36] N. Nagaosa, J. Sinova, S. Onoda, A. H. MacDonald, and N. P. Ong, Anomalous hall effect, Rev. Mod. Phys. **82**, 1539 (2010).

[37] R. D. King-Smith and D. Vanderbilt, Theory of polarization of crystalline solids, Phys. Rev. B **47**, 1651 (1993).

[38] See Supplemental Material at URL-will-be-inserted-by-publisher for additional details.

[39] P. Venezuela, M. Lazzeri, and F. Mauri, Theory of double-resonant raman spectra in graphene: Intensity and line shape of defect-induced and two-phonon bands, Phys. Rev. B **84**, 035433 (2011).

[40] In the notation of Ref. [44], the coupling constant ξ is β^{e-l}/b_0^2, b_0 being the carbon-carbon distance.

[41] H. Suzuura and T. Ando, Phonons and electron-phonon scattering in carbon nanotubes, Phys. Rev. B **65**, 235412 (2002).

[42] S. Piscanec, M. Lazzeri, F. Mauri, A. C. Ferrari, and J. Robertson, Kohn anomalies and electron-phonon interactions in graphite, Phys. Rev. Lett. **93**, 185503 (2004).

[43] T. Sohier, M. Calandra, C.-H. Park, N. Bonini, N. Marzari, and F. Mauri, Phonon-limited resistivity of graphene by first-principles calculations: Electron-phonon interactions, strain-induced gauge field, and boltzmann equation, Phys. Rev. B **90**, 125414 (2014).

[44] O. Bistoni, P. Barone, E. Cappelluti, L. Benfatto, and F. Mauri, Giant effective charges and piezoelectricity in gapped graphene, 2D Materials **6**, 045015 (2019).

[45] B. A. Bernevig and T. L. Hughes, *Topological Insulators and Topological Superconductors* (Princeton University Press, 2013).

[46] S. Konschuh, M. Gmitra, and J. Fabian, Tight-binding theory of the spin-orbit coupling in graphene, Phys. Rev. B **82**, 245412 (2010).

[47] M. Droth, G. Burkard, and V. M. Pereira, Piezoelectricity in planar boron nitride via a geometric phase, Phys. Rev. B **94**, 075404 (2016).

[48] H. Rostami, F. Guinea, M. Polini, and R. Roldán, Piezoelectricity and valley chern number in inhomogeneous hexagonal 2d crystals, npj 2D Materials and Applications **2**, 15 (2018).